Electrochemical Phase Engineering of Li-Ti-P-O Nanocomposite Thin Films

Daniela R. Fontecha*[1], Osma Gomez[3], Nam Soo Kim[4], Sang Bok Lee[1, 3, 4], Gary W. Rubloff[1,2], Keith E. Gregorczyk*[1]

[1]Department of Materials Science and Engineering at University of Maryland, College Park, MD, 20742, USA

[2]Institute for Systems Research at University of Maryland, College Park, MD, 20742, USA

[3]Department of Chemistry and Biochemistry, University of Maryland, College Park, MD, 20742, USA

[4]Maryland NanoCenter, Institute for Research in Electronics and Applied Physics, University of Maryland, College Park, MD, 20742, USA

Key Words:

Thin Film, Nanocomposite, Electrode, High capacity electrode, high frequency electrode, ionic materials, electrochemical phase engineering, NASICON LTP, orthorhombic LTP, lithium titanium phosphate, anatase TiO2, Atomic Layer Deposition, batteries, supercapacitors, microelectronics

Abstract

Nanoscale materials processing advancements have enabled on-chip ionic devices like microbatteries, super capacitors, ion-gated transistors, etc. using standard semiconductor processes (such as atomic layer deposition - ALD) to develop electrochemically active thin films. However, challenges remain in understanding and controlling ionic and electronic transport in nanoscale systems. Nanoscale ionic systems that are tunable at multiple scales (chemical composition, phase distribution, and crystal structure) are critical in understanding how these parameters affect transport and materials properties. In this work we study a system with these qualities and introduce a lever - electrochemical phase engineering - to remove an electrochemically active crystalline phase ($LiTi_2(PO_4)_3$ - LTP) that allows us to understand the effects of individual phases on ionic transport in a quaternary ALD nanocomposite.

We use the Li-Ti-P-O nanocomposite developed by ALD, which consists of crystalline LTP, anatase TiO_2 and an amorphous LTP matrix. Each phase contributes to Li^+ ion storage at different redox potentials, and the crystalline LTP phases are structurally unstable below 0.5 V vs Li^+/Li, allowing the electrochemical removal of the crystalline LTP phase to study its effects on ionic and

electronic transport in the nanocomposite system. We demonstrate the Li-Ti-P-O materials system to be able to switch from high power (60 % capacity retention at an ultrafast charging rate of 200 C) to high capacity (1302 mAh/g at 1 C), making this an interesting material for thin film ionic devices, especially in applications where phase-selectivity provides an advantage.

TOC Figure:

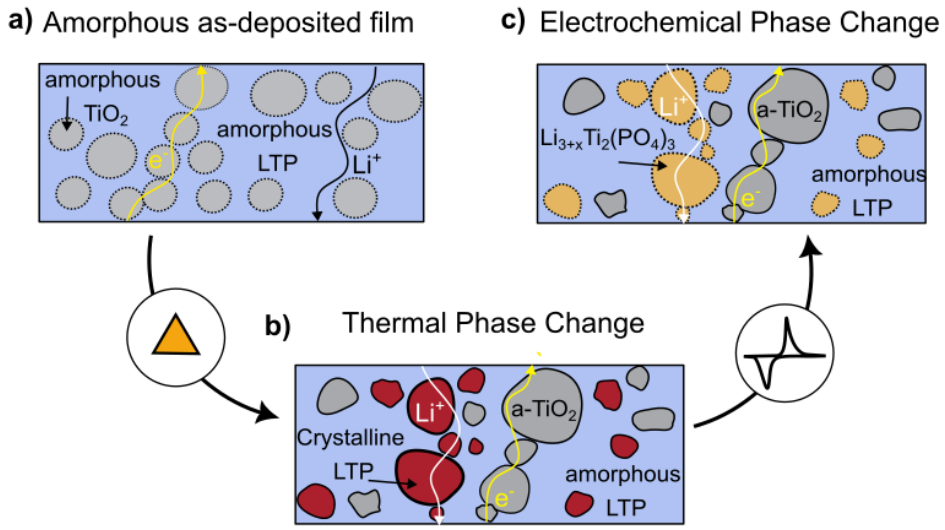

1. Introduction

Within the context of microelectronics, recent advances in semiconductor processing of electrochemically active materials have enabled new classes of thin film devices such as microbatteries, ionic supercapacitors, and ion-gated transistors.[1–3] These devices represent an emerging generation of low-energy, high-power systems that can be embedded within integrated circuits for local energy delivery, sensing, memory, and signal regulation[4–6]. However, a key challenge in advancing these devices is the limited set of design rules for how ionic and electronic transport emerge — and can be tuned — in nanoscale thin film materials systems. Addressing this requires both new synthesis approaches and platforms that allow the relationship between structure, phase distribution, and transport to be studied systematically.

Thin film ionic materials suitable for these emerging applications can best be understood through developments in the well-established field of thin film battery materials. Early work in thin film coatings, enabled by atomic layer deposition (ALD), for lithium ion batteries (LIBs) revealed tradeoffs in intentionally modifying an interface in favor of stable cycling, often at the expense of ion mobility across newly formed interfaces, demonstrated with ALD coatings of Al_2O_3 and lithium phosphorous oxynitride (LiPON) on bulk cathode materials like lithium cobalt oxide.[7,8] These tradeoffs highlight a broader challenge: in thin film ionic systems, interface structure and composition have an outsized impact on transport properties. Designing materials that are tunable in both composition and structure is essential to understanding and controlling that impact.

Though thin-film electrode materials have traditionally been binary compounds (e.g., SnO_2,[9] V_2O_5,[10,11] TiO_2,[12,13] etc.), recent advances have extended ALD to complex chemistries more commonly used as bulk battery materials. $LiFePO_4$, a commercially available LIB cathode, has been realized by ALD through a supercycle scheme combining binary Li_2O and $FePO_4$ processes to achieve the target chemistry.[14] Using a similar supercycle scheme, rhombohedral $LiTi_2(PO_4)_3$ (NASICON LTP), a fast Li^+ ion conductor in bulk, was recently developed by our group as an ALD nanocomposite electrode. This thin film electrode is composed of NASICON LTP and anatase TiO_2 embedded in an amorphous Li-Ti-P-O matrix, analogous to bulk NASICON LTP electrode composites.[15] Critically, this nanocomposite was demonstrated to have high compositional and crystalline phase tunability — qualities that make it a promising platform for studying ionic and electronic transport in confined thin film geometries.

In this work, we exploit that tunability to introduce electrochemical phase engineering as a tool for altering the phase distribution, and therefore the transport properties of the Li-Ti-P-O

nanocomposite. By combining composition-controlled ALD films with voltage-window-selective phase engineering, we drive controlled evolution of crystal structure, phase distribution, and internal interfaces. Most importantly, we use this control to isolate the contribution of each constituent phase to the overall electrochemical behavior of the system.

We demonstrate, through electrochemical phase engineering, a voltage-dependent materials system that can switch from high power to high capacity by removing the crystalline LTP phase. In the high power voltage window (2.1 V – 3.5 V vs Li^+/Li), the nanocomposite retains 60 % of its initial capacity (125 mAh/g) at a charging rate of 200 C (18 sec). In the high capacity voltage window (0.5 V – 3.5 V vs Li^+/Li), the nanocomposite delivers 1302 mAh/g at 1 C and retains 61.9 % of its initial capacity at a charging rate of 20 C (3 min). Together, these results establish the Li-Ti-P-O nanocomposite as a tunable and phase-selective platform for studying how crystal structure and interfaces govern transport in thin ionic films — with direct relevance to thin film microbatteries, ionic supercapacitors, and the broader challenge of integrating ionic nanomaterials into semiconductor device workflows.

2. Experimental Methods

ALD Sample Fabrication. Depositions were conducted at 300 ^oC in a Cambridge Nanotech (now Veeco) Fiji F200 Gen 1 ALD reactor coupled to an ultra-high vacuum (UHV) cluster system ($<10^{-8}$ Torr). ALD precursors were lithium tert-butoxide (LiO^tBu) (synthesized in-house), deionized water, trimethyl phosphate (TMP) (Sigma, 99%), and titanium (IV) isopropoxide (TTIP) (Sigma, 99.99 %) with argon (Airgas UHP, 99.999%) used as the carrier gas. The base pressure of the ALD reactor was $1x10^{-6}$ Torr, and the process pressure was maintained at 200 mTorr by the flow of UHP argon (Airgas, 99.999%) gas. LiO^tBu was synthesized in-house by adding *tert*-butanol (11.94

mL, 124.8 mmol) to 50 mL of hexane. Upon cooling to 0 °C, *n*-butyllithium (11.35 mL, 11 M in hexane solution) was added in an argon atmosphere, and the resulting solution was stirred at room temperature for 2 hours to prepare a LiO^tBu solution. The solution was then dried to yield ~15 g of LiO^tBu as a fine white powder.[16]

The LiO^tBu was kept at 150 ^oC in a stainless-steel bubbler and delivered to the ALD reactor with 40 sccm argon carrier gas flow. H_2O was kept at room temperature, TMP was kept at 70 ^oC, and TTIP was kept at 100 ^oC. H_2O, TMP, and TTIP were all kept in stainless-steel vapor draw cylinders. ALD films were deposited with lithium oxide and titanium phosphate subprocesses with a ratio, *n*, of 2:1 and 7:1 titanium phosphate to lithium oxide (n = 2 and 7, respectively). The lithium oxide subprocess consisted of a 5 second LiO^tBu pulse, and a 0.06 second H_2O pulse. The titanium phosphate subprocess consists of a 0.2 second TMP pulse followed by a 0.06 second water pulse and a 0.1 second TTIP pulse followed by a 0.06 second water pulse. All processes have a 20 s Ar purge after LiO^tBu and TTIP precursor pulses and 10 s Ar purge after the H_2O pulse. With a growth rate of ~ 0.16 Å/min, the 60 nm depositions took 63 hours.

The 60 nm Li-Ti-P-O ALD films were deposited on Si chips with 500 nm thermal SiO_2, 10 nm Ti, and 100 nm Pt (i.e. Si/SiO_2/Ti/Pt stack) patterned by a stainless-steel shadow mask leaving a 0.61 cm^2 deposition area on the center of the chip with the edges of the chip exposed to the Pt layer for electrical contact. These films were annealed in a rapid thermal annealing furnace under a flowing N_2 environment at 650 ^oC for 8.5 minutes and quenched to room temperature to form a semicrystalline nanocomposite containing TiO_2 anatase and LTP NASICON grains embedded in an amorphous Li-Ti-P-O matrix; details about this process are available in a previous publication.[15]

Characterization. Film thickness was measured by cross-sectional imaging of the sample

in a Hitachi SU-70 scanning electron microscope (SEM) with a 10 kV acceleration voltage (**S1**). Film density was measured by X-Ray Reflectometry (XRR) (**S2**). XXR was performed by a Rigaku X-ray diffractometer in a grazing-incidence configuration in continuous scan mode with a step size of 0.003 degrees and 2 s counting time. Grazing incidence X-ray diffractometry (GI-XRD) was performed by a Rigaku X-ray diffractometer for the pre-cycled film in **Figure 1b** and a PANalytical XPert Pro MRD X-ray diffractometer for the post-cycled film in **Figure 5b** (due to tool availability at the time). Both diffractometers were in a grazing-incidence configuration with a scan rate of 0.025 °/s and a step size of 0.05° and a Cu-Kα (λ= 1.54 Å) radiation source.

Surface film composition was measured by X-Ray Photoelectron Spectroscopy (XPS) (**S3**). Post deposition, films were transferred under UHV to a Kratos Ultra DLD Surface Analysis system ($1x10^{-9}$ Torr) for XPS analysis. XPS data were collected using a monochromatic Al Kα (1486 eV) X-ray source at 15 kV and a total anode power of 150 W. Survey spectra were collected with a pass energy of 160 eV and binding energy step size of 1 eV. High resolution spectra were collected with a pass energy of 20 eV and a binding energy step size of 0.1 eV at the appropriate number of scans to produce a satisfactory signal/noise ratio. Casa XPS was used to analyze all data. XPS peaks were fitted using a Shirley background and 30/70 Gaussian/Lorentzian pseudo-Voigt functions. Elemental quantification was done by comparing the ratios of high-resolution peak areas with the tabulated Kratos relative sensitivity factors. All spectra were charge calibrated to the C 1s peak at 284.8 eV.

Crystalline phases in the film were measured by Raman spectroscopy. Raman measurements were conducted in air with a “Labram HR” microscope system (Horiba Jobin Yvon USA). A 633 nm laser (HeNe) with a D1 intensity filter was used. The incident laser power was

controlled to 1 mW and ~2 μm diameter spot size with a 100X microscope objective. A 600 gr/mm grating was used for acquisitions with 20 s exposure and 5 repetitions.

Electrochemical Characterization. All cells were cycled in a 1 M $LiClO_4$ in propylene carbonate liquid electrolyte cell against lithium metal and the 60 nm Li-Ti-P-O film as the working electrode. Electrochemical cycling experiments were performed using a Biologic VSP potentiostat. All electrochemical measurements were taken at a room temperature of 21 ^oC. The samples cycled within the voltage window of 1.2 V – 3.5 V vs Li^+/Li were cycled in a two-electrode beaker cell with an active area of 0.61 cm^2 and cycled in an argon-filled glove box. The samples that were cycled down to 0.25 V and 0.5 V vs Li^+/Li were cycled in an air-tight three-electrode T-cell, designed such that the backside of the Si chip is not exposed to the electrolyte. The T-cell configuration was used for samples cycled down to low potentials to ensure that the sides of the Si chip were not contributing to the redox activity. The active area of samples in T-cells is 0.283 cm^2, controlled by the inner diameter of the silicone gasket between the sample and a stainless-steel cap (see **S4** for more details on this experimental setup). For specific capacity calculations, the film thickness of 60 nm (**S1**), the measured film density (2.9 g/cm^3) from XRR results (see **S2**) and the exposed surface area of the respective electrochemical cell setup were used to calculate the total mass of the film participating in the electrochemistry during galvanostatic cycling. The A/g method was used to calculate C-rates due to the ambiguity of theoretical capacities in the Li-Ti-P-O film containing three or more distinct phases. To address this, the C-rate was determined by galvanostatically cycling a sacrificial sample at each voltage window reported and determining the required current density to charge or discharge the film over that voltage range in 1 hour. This is how the 1 C rate is defined for all experiments, and all areal current densities are provided in the manuscript, with gravimetric current densities provided in the SI (**S5**).

3. Results and Discussion

3.1 Proposed Electrochemical Phase Engineering Process

This work examines ionic transport and storage in confined nanocomposite Li-Ti-P-O ALD thin films using a previously published synthesis method.[15] As detailed in the methods (Section 2), two film compositions are studied in this work to probe the effects on the availability of lithium and phosphate during the early stages of LTP crystallization. The film compositions were tuned by changing the ratio, *n*, between titanium phosphate and lithium oxide ALD sub-cycles. For n = 2, the as-deposited composition is $\mathbf{Li_{6.6}Ti_2(PO_4)_3}O_3C_{1.2}$ (denoted as "Li-rich") and for n = 7, the as-deposited composition is $\mathbf{Li_{1.5}Ti_2(PO_4)_3}\bullet Ti_{2.5}O_{6.9}C_{3.9}$ (denoted as "Li-poor") - both verified with XPS (see figure **S3** in supplemental).

Scheme 1 presents an overview of the sequence of processing steps involved in synthesizing and phase-engineering the Li-Ti-P-O nanocomposite that will be discussed in this work. Beginning with the synthesis of this material, ***Scheme 1a*** depicts the morphology of the amorphous as-deposited ALD film determined by XPS (**S3**) and EIS (**S6**). Then the as-deposited ALD film is crystallized via rapid thermal annealing at 650 ^oC for 8.5 minutes (***Scheme 1b***), nucleating both anatase TiO_2 and crystalline LTP in an amorphous LTP matrix. ***Scheme 1a-b*** are derived from the conclusions of our previous publication detailing the morphology of the LTP nanocomposite system.[15] Lastly, we demonstrate the final transition (***Scheme 1c***), which occurs electrochemically by sweeping an electrochemical cell to potentials below 0.5 V vs Li/Li^+ where the crystalline LTP irreversibly forms an amorphous $Li_{3+x}Ti_2(PO_4)_3$ phase. This work will first walk through the structural characterization of the annealed Li-Ti-P-O nanocomposite film depicted in **Scheme 1b**

(Section 3.2), followed by electrochemical characterization of the films depicted in **Schemes 1b-c** individually (Section 3.3), and will conclude with analysis of the effects of crystalline phase on transport kinetics (Section 3.4).

Scheme 1. Progression of phase engineering of Li-Ti-P-O nanocomposite (60 nm thick) from a) ALD deposition to b) thermal annealing and c) electrochemical phase engineering.

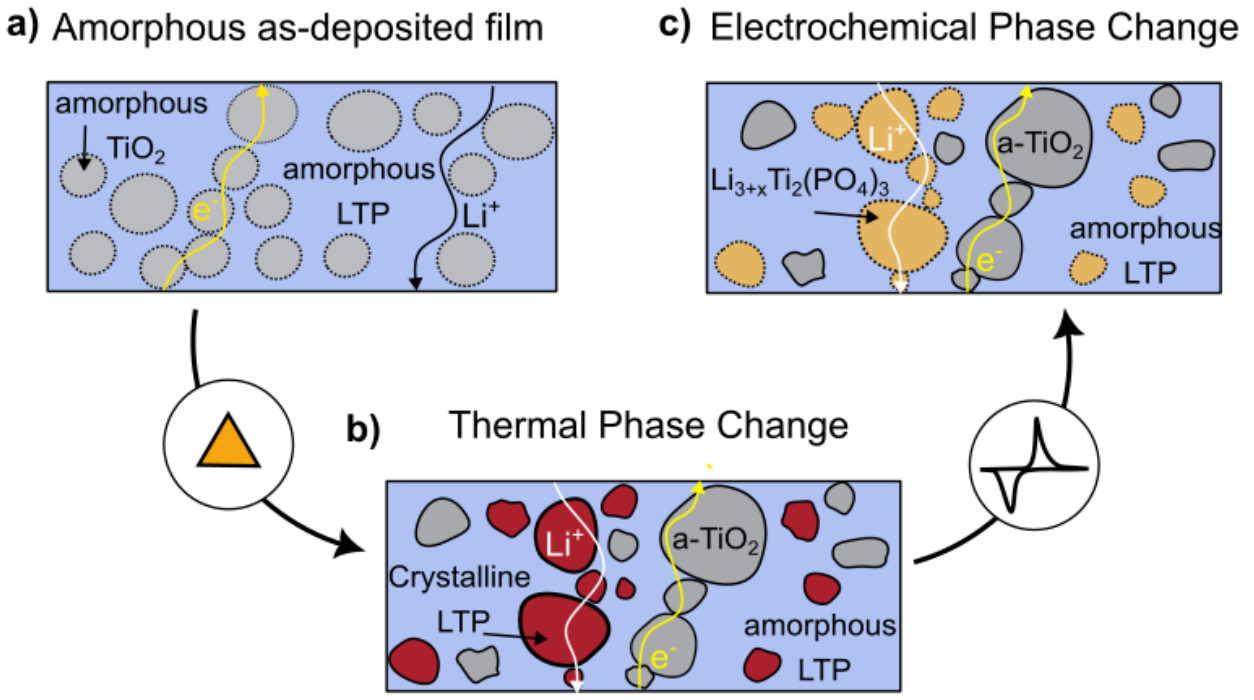

3.2 Structural Characterization

In order to determine and understand the transport properties we first determine the structure and composition of the thin-film materials. Figure **1a** shows the corresponding Raman spectroscopy of both the Li-rich and Li-poor films after annealing. These data confirm the presence of anatase TiO_2 denoted by peaks at 143, 396, 515 and 637 cm^{-1}.[17] Both compositions also exhibit a broad bump between ~ 910 and 1050 cm^{-1}, commonly ascribed to be the "NASICON

fingerprint region" that is often used to identify the NASICON $LiTi_2(PO_4)_3$ structure with R$\underline{3}$c spacegroup.[18] However, there is a notable difference in profiles between 910 - 1050 cm^{-1} in the Li-rich and Li-poor Raman spectra that indicates the LTP is taking on a different structure at early stages of crystallization. The Li-rich sample develops a broad peak with higher intensities towards the right, matching the reference spectrum of a more crystalline Li-Ti-P-O nanocomposite (annealed at 850 ^oC for 3 hrs and quenched to room temperature).[15] The Li-rich sample shows additional broad features at 230-292, 349, and 437 cm^{-1} that align with the NASICON LTP Raman active modes. In contrast, the Li-poor sample has an inverse profile in the 910 - 1050 cm^{-1} region and is missing the features that align with the NASICON LTP Raman-active modes, indicating that the initial composition of the films directs the early stages of LTP crystallization towards different structures. To better understand what these changes in the Li-poor sample correspond to, we will look to grazing incidence X-ray diffraction (GI-XRD) to assign a structure to these features in the Li-poor sample.

Figure 1b shows the GI-XRD spectra of the Li-rich and Li-poor compositions in this work. The Li-rich GI-XRD reflections match very well with crystalline NASICON LTP and anatase TiO_2, as predicted by the TEM-SAED performed on films with this exact composition and processing.[15] However, new reflections appear as shoulders at 21.9^o and 27.2^o 2θ in the Li-poor films, hinting at formation of orthorhombic LTP rather than NASICON LTP.[19,20] NASICON and orthorhombic LTP are quite similar in structure, both composed of a $[Ti_2(PO_4)_3]$ backbone that is connected by corner sharing between PO_4 tetrahedra and TiO_6 octahedra to form a 3D network of interstitial sites for Li^+ ion conduction. In orthorhombic LTP the backbone units alternate in orientation, creating additional reflections emerging at 21.9^o and 27.2^o 2θ. Though NASICON LTP and orthorhombic

LTP (space group Pbca) differ slightly in structure, they can offer similar Li^+ ion conductivities depending on Li-concentration in the orthorhombic LTP structure.[19]

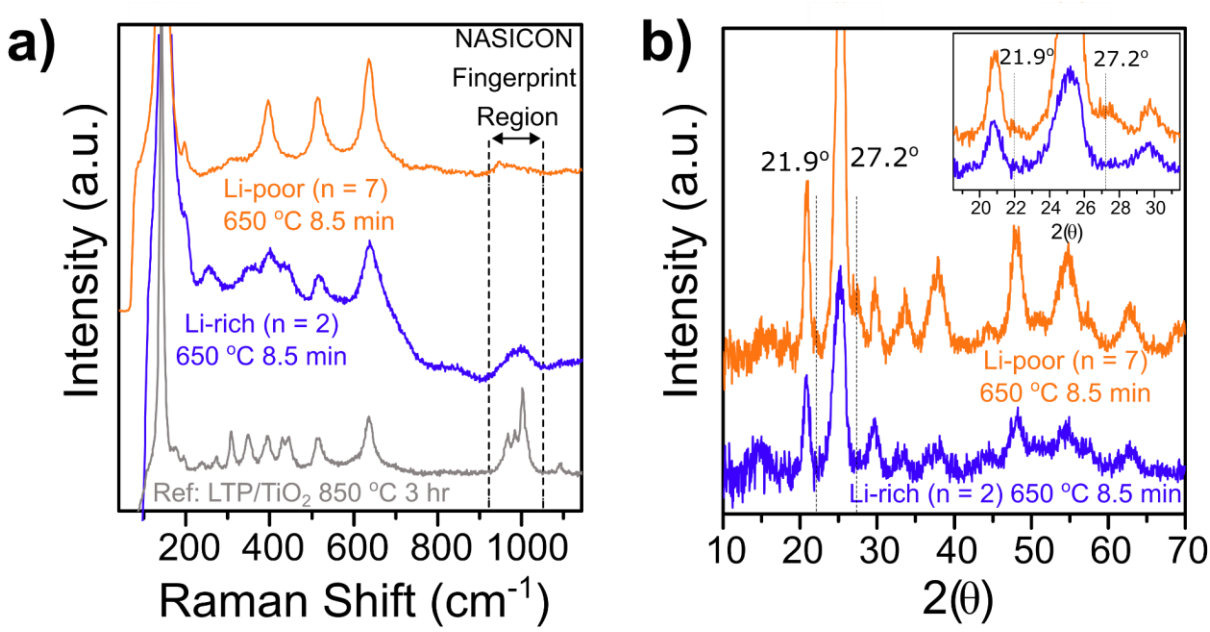

Figure 1. a) Raman spectroscopy and b) grazing incidence-X-ray diffractometry of Li-rich (purple) and Li-poor (orange) Li-Ti-P-O ALD nanocomposite thin films rapid thermal annealed at 650 °C for 8.5 minutes.

Here, we demonstrate a degree of control over the phases present in this quaternary phase nanocomposite by changing the initial composition of the films followed by thermal annealing. However, additional verification of the orthorhombic LTP structure is required to corroborate the GI-XRD results of this semicrystalline nanocomposite. Both NASICON and orthorhombic LTP are known to be redox-active species as long as there is an external electron-conduction pathway to enable the redox reaction.[20,21] We have already reported this to be the case with this nanocomposite structure, where the anatase TiO_2 provides the electron conduction pathway in the system.[15] In the following section (3.3.1), we will continue to probe the phase composition of these films with techniques like cyclic

voltammetry, which can be more sensitive to phase transitions in redox-active materials than Raman spectroscopy or GI-XRD.

3.3 Electrochemical Materials Properties

3.3.1 Crystalline LTP Voltage Window (1.2 V - 3.5 V vs Li^+/Li)

As discussed in the introduction and demonstrated in Section 3.2, materials characterization shows we have a quaternary phase system**.** Crystalline LTP (NASICON or orthorhombic), anatase-TiO_2, and amorphous LTP.

We can control the ratio of these materials through the following;

1. **ALD Deposition** - we can tune the composition to be Li-rich or Li-poor by tuning the ratio between ALD sub-process of lithium oxide and titanium phosphate using a previously published process.[15]
2. **Thermal Annealing** - we can grow crystalline LTP and TiO_2 nanocrystals, forming a mixed crystalline nanocomposite with crystalline LTP and anatase-TiO_2 in an amorphous Li-Ti-P-O matrix. Section 3.2 showed the composition-controlled phase engineering capabilities of this system in early stages of crystallization. This section (3.3.1) will show the nanoscaling effects on thermodynamic equilibrium states in the Li-rich and Li-poor films with electrochemical techniques.
3. **Electrochemical Cycling -** As will be shown in section 3.3.2, cycling the nanocomposite below 0.5 V vs Li^+/Li results in a phase change from crystalline to amorphous LTP. Therefore, using electrochemical techniques, we can further control the redox-active phases present in the nanocomposite.

Together, tuning these parameters and the resulting materials properties encompass

what electrochemical phase engineering, i.e. using the added electrochemical functionality to further manipulate material phase and crystal structure.[22] Using these techniques, we can control the materials properties of the composite film and can attribute the contributions from each phase to the overall transport properties in nanoscale ionic/electronic composite systems.

To probe the nature of the redox-active crystalline LTP phases identified in Section 3.2, the Li-poor and Li-rich samples were cycled electrochemically between 1.2 – 3.5 V vs Li^+/Li where the orthorhombic and NASICON LTP phases are redox active.[20,21] **Figure 2** shows the cyclic voltammogram (CV) of the Li-poor sample, identified with GI-XRD to contain orthorhombic LTP.[20,21,23,24] The first and fourth cycle at 0.2 mV/s are nearly identical to each other, demonstrating early stage reversibility. This indicates that intimate contact is maintained between the amorphous matrix and crystalline grains, even after multiple cycles.[25] There is a lithium insertion peak at 1.70 V vs Li^+/Li and extraction peak at 1.95 V vs Li^+/Li that correspond to lithiation/delithiation of anatase TiO_2.[24] A small redox pair is also present at 1.42 V and 1.65 V vs Li^+/Li that matches redox activity of rutile TiO_2,[26] indicating a trace amount present. The relatively small anatase redox pair polarization (peak separation of 240 mV) can be attributed to reduced diffusion lengths and increased active area that comes with the small grain sizes (ranging from 5-40 nm in diameter) found in this nanocomposite.[15,27]

At voltages above the TiO_2 redox couple, three redox pairs (centered at 2.25 V, 2.45 V and 2.80 V vs Li^+/Li) are present. **Figure 2** shows a dominant 2.8 V vs Li^+/Li peak and relatively lower intensity 2.45 V and 2.25 V vs Li^+/Li peaks - identical in profile to the redox peaks for orthorhombic LTP reported in literature.[20,28] This is in agreement with GI-XRD of the Li-poor chemistry shown in **Figure 1b**, where evidence of orthorhombic LTP is observed by the new reflections at 22.9° and

27.2° 2θ. Structural and electrochemical observations indicate that the Li-poor initial composition paired with thermal annealing presents the conditions for orthorhombic LTP crystallization rather than NASICON LTP - in agreement with observations by Wang et. al. in 1992 that varying initial lithium content during crystallization can form either NASICON or orthorhombic LTP.[29]

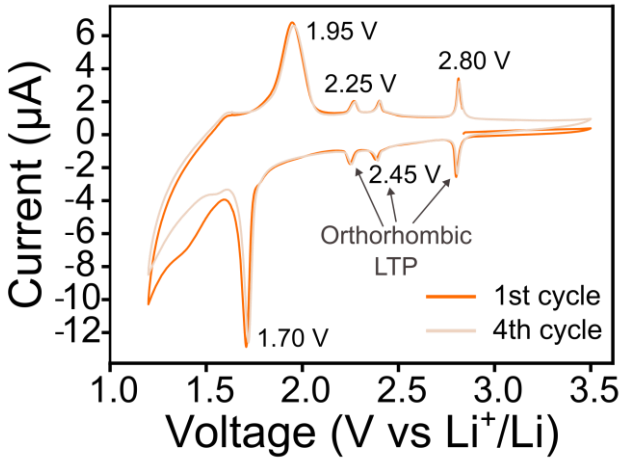

Figure 2. Cyclic voltammetry of Li-Ti-P-O (Li-poor) annealed at 650 °C for 8.5 min as the working electrode in a beaker cell with lithium metal as the counter and reference electrodes, cycled at 0.2 mV/s between 1.2 V – 3.5 V vs Li^+/Li.

Likewise, **Figure 3** shows the CV results of the Li-rich sample cycled between 1.2 V - 3.5 V vs Li^+/Li at 0.2 mV/s. Again, this sample shows very good reversibility between cycles and similar TiO_2 Li^+ insertion and extraction peaks at 1.95 V and 1.70 V vs Li^+/Li, respectively. However, the LTP-related redox peaks take on a different profile, indicating a change in structure of the LTP phase. The 2.45 V vs Li^+/Li peak is now the dominant peak, followed by a smaller peak at 2.80 V vs Li^+/Li and a small shoulder at 2.25 V vs Li^+/Li. This change in redox activity indicates that the crystalline LTP in the Li-rich sample is not predominantly orthorhombic but rather in the NASICON phase.[30] It is important to note that stoichiometric NASICON $LiTi_2(PO_4)_3$ typically undergoes a single step 2-electron transfer process with a single redox potential at 2.5 V vs Li^+/Li to form $Li_3Ti_2(PO_4)_3$ rather than the multiple peaks observed in **Figure 3**.[21] Understanding the source of the 2.80 V vs Li^+/Li redox peak requires a deeper dive into the redox behavior of the NASICON

structure.

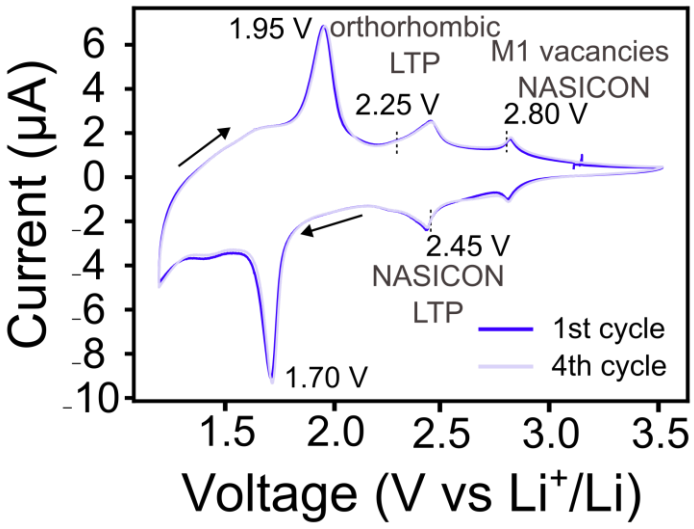

Figure 3. Cyclic voltammetry of Li-Ti-P-O (Li-rich) annealed at 650 °C for 8.5 min as the working electrode in a beaker cell with lithium metal as the counter and reference electrodes, cycled at 0.2 mV/s between 1.2 V – 3.5 V vs Li^+/Li.

The NASICON LTP structure consists of corner sharing TiO_6 octahedra and PO_4 tetrahedra that form a rhombohedral backbone structure with two different types of interstitial sites, commonly labelled M1 and M2.[21,30,31] In NASICON $LiTi_2(PO_4)_3$ Li^+ ions fully occupy only the M1 interstitial sites. The NASICON structure can be lithiated at 2.5 V vs Li^+/Li in a single step two-phase process, in which Li^+ ions intercalate into the M2 sites followed by cooperative migration of the Li^+ ions from M1 to M2 sites until a composition of $Li_3Ti_2(PO_4)_3$ is achieved. In its fully lithiated state, $Li_3Ti_2(PO_4)_3$ is in a distorted rhombohedral structure with Li^+ ions now only found in M2 sites.[23,30] The redox peak at 2.45 V vs Li^+/Li in **Figure 3** demonstrates the expected behavior of Li^+ ions entering the M2 sites of the NASICON LTP structure. However, the presence of the other peak and shoulder in **Figure 3** (2.8 V and 2.25 V V vs Li^+/Li, respectively) indicates that there are some structural deviations in the NASICON LTP grains that are more sensitive to cyclic voltammetry than the other structural characterization methods (i.e., GI-XRD, Raman

spectroscopy, and transmission electron microscopy selected area electron diffraction) used in this work and previous work on the ALD Li-Ti-P-O nanocomposite films.[15] There are two possible structural explanations for the redox pairs at 2.25 V and 2.80 V vs Li^+/Li:

1. there exist stable Li^+ ion vacancies in the M1 sites of the NASICON LTP structure,[30,32,33]
2. or the LTP crystalline grains are actually in an orthorhombic rather than NASICON crystal structure.[20,23]

The use of crystallographic techniques like GI-XRD for direct verification of hypothesis (1) is complicated by the low crystallinity of this sample and low X-ray scattering factor of lithium preventing precise calculation of lattice parameters and Li^+ ion location.[30] However, as shown in **Figure 1b**, the reflections that line up with the orthorhombic structure are not detected in the Li-rich sample. This suggests that the majority of the crystalline LTP of the Li-rich film is in the NASICON form and stabilized in a locally lithium-deficient NASICON composition ($Li_{1-x}Ti_2(PO_4)_3$) that accounts for the M1 vacancy redox pair at 2.80 V vs Li^+/Li.[30,32–34] The orthorhombic crystal structure appears to be only a minority phase, below the GI-XRD instrument detection limit, designated in cyclic voltammetry by the small shoulder at 2.25 V vs Li^+/Li (**Figure 3**).[20]

The emergence of the 2.8 V vs Li^+/Li peak (and corresponding M1 vacancies) in NASICON LTP is more commonly observed in reports with bulk synthesis techniques that enable LTP nanoparticles (50-100 nm) to form, which tend to perform better in terms of long-term stability and rate retention.[20,33,35] A possible explanation is that in electrodes where the NASICON LTP grains approach the nanoscale, the energy landscape is altered by local stresses and interfacial energy that may alter the equilibrium composition at the interfaces. Such nanosizing effects on local stress and strain at interfaces have been known to alter equilibrium phases in cathode

materials like V_2O_5.[8,36] In the case of this work, the Li-Ti-P-O nanocomposite contains LTP particles in the range of 5-40 nm in diameter[15] - well within the range for this observed behavior of vacancy formation due to microstructure.

The relative dominance of these nanostructuring effects (M1 vacancy stabilization in NASICON LTP vs orthorhombic LTP nucleation and growth) depends on the initial composition of the ALD film and can be determined by cyclic voltammetry as shown in **Figures 2 & 3**. The CV and GI-XRD results in this work show that Li-poor films preferentially nucleate orthorhombic LTP while Li-rich films predominately nucleate NASICON grains with M1 vacancies at the interface when annealed. Therefore, composition control through ALD supercycling provides a fine-tuned knob for phase engineering of the Li-Ti-P-O nanocomposite platform.

3.3.2 Electrochemical Phase Change at Low Potentials vs Li^+/Li

Figure 4 shows the cyclic voltammetry (CV) of the Li-rich (NASICON LTP) (**Figure 4 a-b**) and Li-poor (orthorhombic LTP) (**Figure 4 c-d**) nanocomposites cycled from 0.25 V - 3.5 V vs Li^+/Li and 0.5 V to 3.5 V vs Li^+/Li, respectively. The lower limit of the Li-poor sample was simply raised by 0.25 V vs Li^+/Li as a precaution against solid-electrolyte interphase (SEI) formation in the cell. The Li-rich sample (**Figure 4a,b**) has the NASICON LTP reduction peaks in the first lithiation cycle, at 2.45 V and 2.8 V vs Li^+/Li that were determined in **Section 3.3.1** to represent NASICON nanocrystals with stabilized M1 vacancies. However, in subsequent cycles the NASICON LTP redox peaks broaden and eventually disappear. This behavior has been observed in bulk NASICON LTP electrode systems in which cycling below 1 V vs Li^+/Li leads to irreversible vitrification of the NASICON LTP structure.[23,37] The first cycle has a strong peak at 0.5 V vs Li^+/Li suggesting SEI formation caused by the degradation of the liquid electrolyte (1 M $LiClO_4$ in propylene carbonate)

on the nanocomposite surface.[38] However, the 0.5 V vs Li^+/Li peak is not present in the subsequent cycles, indicating a stable electrode/electrolyte interface. Instead, a reversible redox pair is present at 0.80 V vs Li^+/Li representing the Ti(III)/Ti(II) redox couple indicating a phase transition from NASICON LTP to a new redox active $Li_{3+x}Ti_2(PO_4)_3$ phase.

The Li-poor nanocomposite, shown in **Figures 4c,d** exhibits similar behavior of the crystalline LTP (in this case orthorhombic) peaks disappearing after multiple cycles over the full voltage window. In the first cycle, peaks appear at 2.25 V, 2.45 V, and 2.8 V vs Li^+/Li representing the lithiation of orthorhombic LTP.[20] Like in **Figure 4a**, there is a redox peak at 0.85 V vs Li^+/Li in the Li-poor sample CV, indicating a Ti(III)/Ti(II) transformation upon further lithiation. The orthorhombic LTP redox peaks synchronously decrease in intensity and broaden with increasing cycle number, indicating a similar structural instability of the lesser studied orthorhombic LTP below 1 V vs Li^+/Li as has been reported in literature for the NASICON LTP structure.

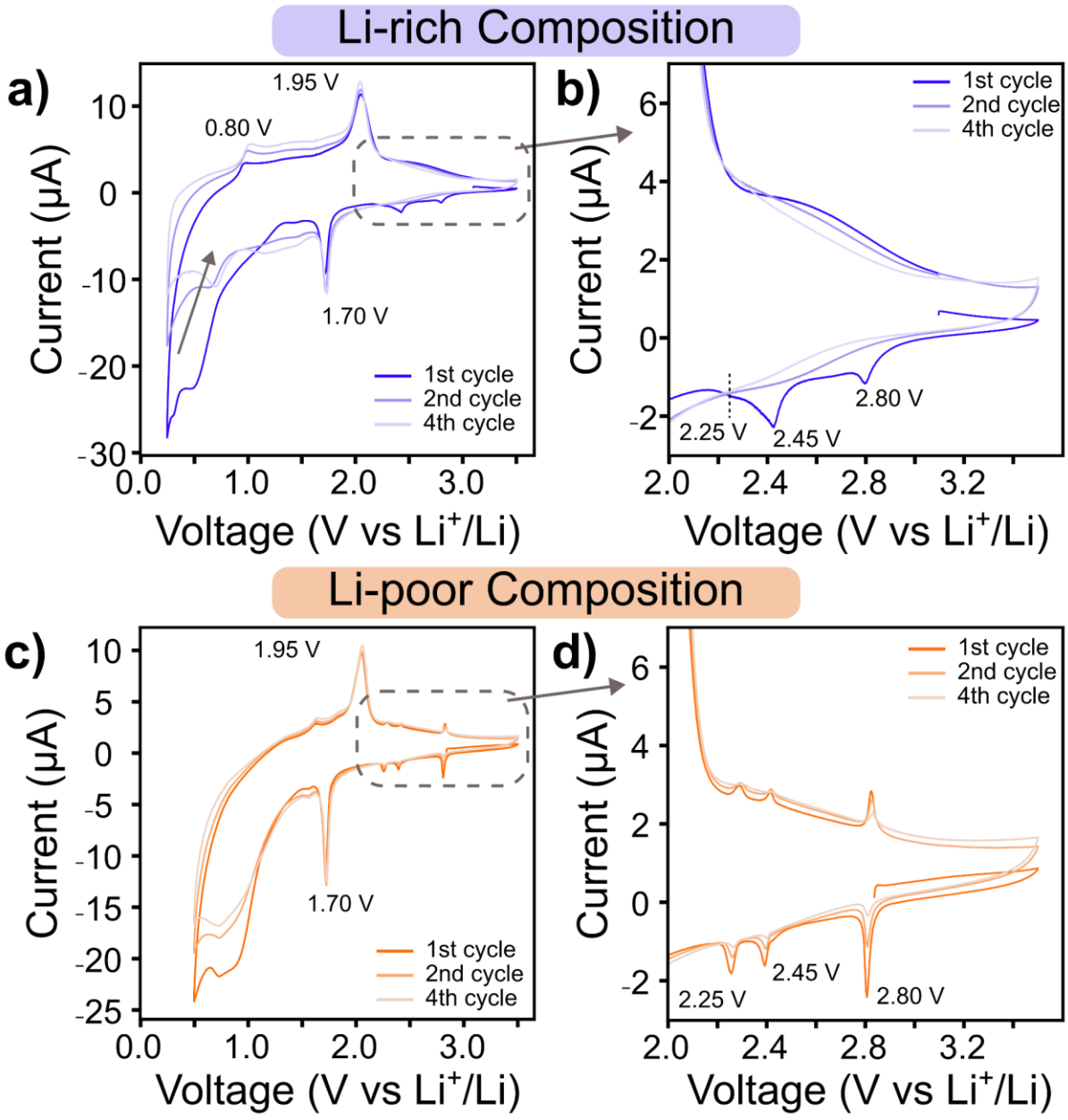

Figure 4. Li-Ti-P-O Li-rich (a,b) and Li-poor (c,d) films annealed at 650 °C for 8.5 min. a) Li-rich film cycled in a T-cell with lithium metal as the counter and reference electrodes, cycled at 0.2 mV/s between 0.25 V – 3.5 V vs Li^+/Li. b) The zoomed in graph of the dashed box region in (a). c) Li-poor film cycled in a T-cell with lithium metal as the counter and reference electrodes, cycled at 0.2 mV/s between 0.5 V – 3.5 V vs Li^+/Li. d) The zoomed in graph of the dashed box in (c).

Raman spectroscopy was performed on the Li-poor nanocomposite before and after electrochemical cycling as shown in **Figure 5a**. The post-cycled sample was de-lithiated by applying a 72 hr hold at 3.5 V vs Li^+/Li such that a steady state current was achieved in the delithiated state before taking the Raman spectra. Before cycling, the Raman spectrum of the Li-

poor sample is similar in profile to **Figure 1a**, with predominant anatase TiO_2 peaks (145, 397, 515, and 637 cm^{-1}) and a left-leaning asymmetric broad peak within the NASICON fingerprint region (~900-1070 cm^{-1}). However, after cycling to low potentials, the Raman spectrum is muted in the NASICON fingerprint region, with small peaks at 944 and 1088 cm^{-1} which indicate a phase transition from orthorhombic LTP to the $Li_{3+x}Ti_2(PO_4)_3$ phase. This work demonstrates that like the NASICON LTP phase, orthorhombic LTP (a less-studied polymorph of LTP) is also structurally unstable against over-lithiation and undergoes a phase transition into what can best be described as $Li_{3+x}Ti_2(PO_4)_3$ glass-like phase as shown in **Scheme 1c**.[23,37]

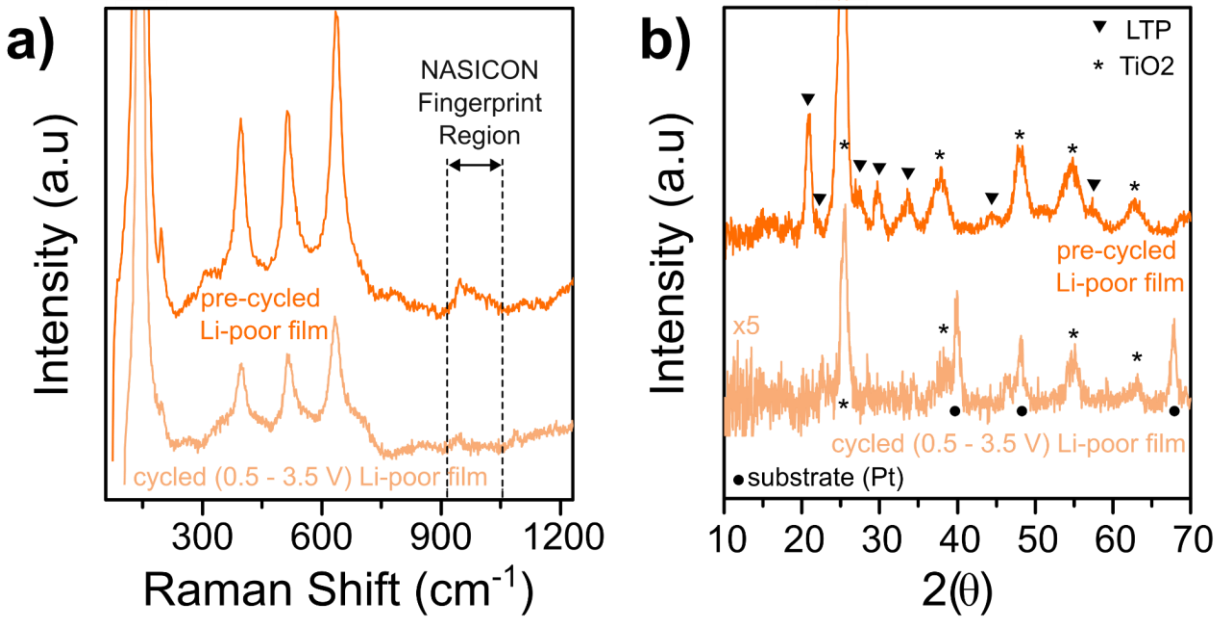

Figure 5. a) Raman and b) GI-XRD spectra of the uncycled Li-poor film (top) and cycled film (bottom) taken out at 3.5 V vs Li^+/Li. The GI-XRD spectra are labeled with reference values from for peaks related to orthorhombic LTP (▼)[20], anatase TiO2 (*, PDF card 21-1272) and the Pt substrate under the cycled film (●, PDF card 03-065-2868).

GI-XRD was also performed on the post-cycled Li-poor LTP film and compared directly to the pre-cycled GI-XRD from Section 3.2, as shown in **Figure 5b**. The preferred substrate for GI-XRD measurements on these nanocomposites is Si because it does not have reflections that

overlap with our sample. However, the post-cycled sample needed to be on Pt to be able to perform the electrochemical experiments and therefore displays peaks at 39.9°, 48.2°, and 67.8° 2θ that come from the Pt substrate, marked with a filled in circle. Both pre- and post-cycled samples show reflections that correspond to anatase TiO_2 (at 25.5°, 37.8°, 46.4°, 54.7°, and 63.0° 2θ, marked by stars) while only the pre-cycled sample shows the reflections that correspond to orthorhombic LTP (20.8°, 21.9°, 27.2°, 29.7°, 33.7°, 44.2°, and 57.6° 2θ, marked by triangles). These results provide strong crystallographic evidence of a loss of the orthorhombic LTP phase driven by electrochemical lithiation of the orthorhombic structure at low potentials (0.5 V vs Li^+/Li), which agree with the disappearance of the orthorhombic redox peaks in cyclic voltammetry (**Figure 4b,c**) and the disappearance of the phosphate Raman peaks in **Figure 5a**.

A key feature of this nanocomposite material is that phase engineering is possible in two distinct ways that affords materials property tunability for a variety of ionic device & microelectronics applications. Summarized in ***Scheme 1*** is the progression of morphological changes with thermal and electrochemical phase engineering, going from the as deposited ALD film (***Scheme 1a***) to the nanocomposite with crystalline LTP by thermal annealing (***Scheme 1b***) to the nanocomposite without crystalline LTP by electrochemical phase engineering (***Scheme 1c***). Thus far in this work, we have studied the electrochemical properties of the Li-Ti-P-O nanocomposite in two main structural configurations:

1. That shown in ***Scheme 1b***, which is achieved by annealing the Li-rich or Li-poor samples at 650 °C for 8.5 minutes and is electrochemically stable between 1.2 V - 3.5 V vs Li^+/Li.
2. That shown in ***Scheme 1c*** is achieved by cycling the annealed samples down < 0.5 V vs Li^+/Li, and is electrochemically stable between 0.25 V - 3.5 V vs Li^+/Li.

Despite the loss of the orthorhombic LTP and NASICON LTP crystal structures in the

transformation to ***Scheme 1c*** morphology, there is still a significant contribution to the overall capacity coming from the anatase grains, the newly formed $Li_{3+x}Ti_2(PO_4)_3$ phase, and pseudocapacitance from the amorphous matrix. Each voltage window in which this system operates offers tradeoffs in capacity and transport, as will be shown in section 3.4, where we detail the consequences of structural composition on transport kinetics and energy storage properties.

3.4 Rate Behavior and Kinetics

The Li-Ti-P-O nanocomposite studied in this work is a complex quaternary material system with three to four distinct phases (depending on processing and operating conditions as highlighted in ***Scheme 1***), each participating in the electrochemical reactions at different redox potentials. The following section aims to understand the kinetic behavior at fast charging rates and its dependence on the redox active phases present (phase-selective by the voltage window). Of particular interest is isolating the effects of the crystalline orthorhombic LTP phase on fast charging capabilities of this nanocomposite, as this is a relatively less-studied phase in lithium titanium phosphate polymorph literature.

3.4.1 Kinetic Behavior of Li-Ti-P-O Nanocomposite with Orthorhombic LTP Grains

Figure 6a shows the rate-retention behavior of the Li-poor nanocomposite cycled in the crystalline LTP-stable voltage window (1.6 V – 3.5 V vs Li^+/Li) between discharge rates of 1 and 20 C for 10 cycles at each current density. The capacity at 1 C (5 $\mu A/cm^2$) is initially 317 mAh/g and gradually decreases with an increasing C-rate. At 20 C (100 $\mu A/cm^2$) the nanocomposite retains 69.7 % of its initial capacity (221 mAh/g), indicating that interfacial reactions and mass transport remain relatively fast at high charging rates. Additionally, the capacity fully recovered

to 316 mAh/g after returning to a 1 C charging rate, showing no signs of degradation.

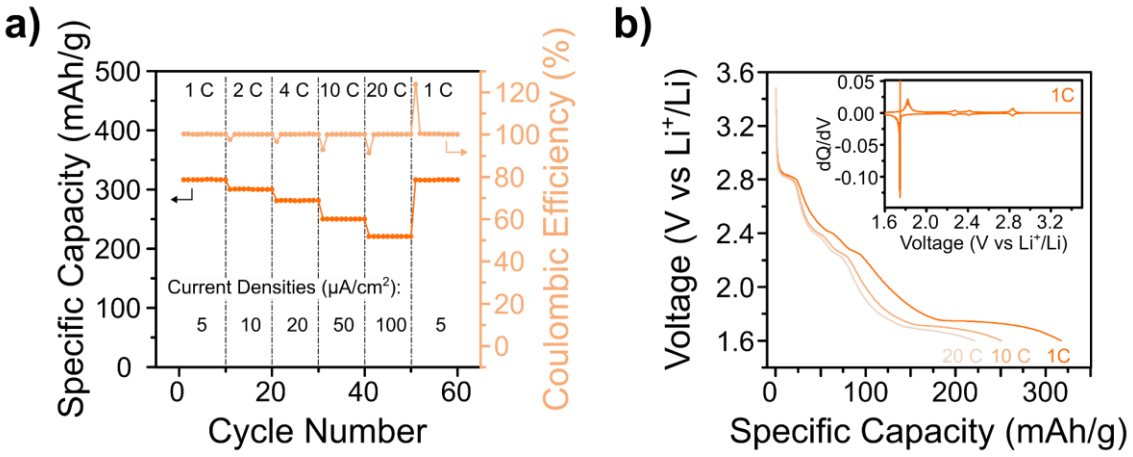

Figure 6. a) Rate retention results for thermal Li-Ti-P-O (Li-poor) annealed at 650 °C for 8.5 minutes cycled in a beaker cell vs lithium metal in 1M $LiClO_4$ in propylene carbonate liquid electrolyte between 1.6 V – 3.5 V at charging rates of 1C (5 μA/uA/cm^2), 2C (10 μA/uA/cm^2), 4C (20 μA/uA/cm^2), 10C (50 μA/uA/cm^2), and 20 C (100 μA/uA/cm^2). b) Galvanostatic discharge curves of the 10th cycle in the series for 1 C, 10 C, and 20 C rates. The inset is a representative dQ/dV curve of this voltage window taken from the 1 C discharge curve.

Figure 6b shows the discharge curves at 1, 10, and 20 C (5, 50, 100 μA/cm^2, respectively) for the same voltage window. As the rates increase from 1 C to 20 C the capacity drops from 317 mAh/g to 221 mAh/g. However, by looking at the plateaus at each rate, it is apparent that not every phase is contributing equally to capacity loss. ***Table 1*** shows the quantification of the capacity loss in the individual phases present, which were calculated by integrating the dQ/dV peaks of these discharge curves while excluding the pseudocapacitive background (as shown in **S7**). At 1C the orthorhombic LTP, anatase TiO_2, and amorphous phases each contributed 48.7, 99.2, and 166.1 mAh/g, respectively. At 20 C the corresponding capacities were 46.0, 62.5, and 120.3 mAh/g, respectively. The capacity analysis at a 20 C charging rate revealed a loss (relative to a 1 C rate) of 36.7 mAh/g (37 %) in the anatase TiO_2 phase and 45.8 mAh/g (27.6 %) in the amorphous matrix whereas there is only a loss of 2.7 mAh/g (5.5 %) in the orthorhombic LTP

phase (with peaks at 2.8 V, 2.45 V and 2.25 V vs Li^+/Li). This points to particularly fast kinetics of the crystalline orthorhombic LTP phase relative to the TiO_2 and amorphous phases in this voltage window. In Section 3.3.4, we will show the impressive kinetic capabilities of the orthorhombic LTP by narrowing the voltage window to exclude TiO_2 redox activity, demonstrated here to be a limiting factor in capacity retention at faster rates.

***Table 1**. Summary of capacity losses experienced by each phase at a charging rate of 20 C compared to 1 C in Li-poor films cycled between 1.6 V - 3.5 V vs Li^+/Li.*

Charge Rate	*Orthorhombic LTP Capacity (mAh/g)*	*Capacity Loss (%)*	*Anatase TiO_2 Capacity (mAh/g)*	*Capacity Loss (%)*	*Amorphous Matrix Capacity (mAh/g)*	*Capacity Loss (%)*
1 C	48.7 (1.7)	-	99.2 (3.4)	-	166.1 (5.7)	-
20 C	46.0 (1.6)	5.5	62.5 (2.1)	37	120.3 (4.1)	27.6

3.4.2 Kinetic Behavior of Li-Ti-P-O Nanocomposite without Crystalline LTP Grains

The Li poor nanocomposite without orthorhombic LTP grains (see ***Scheme 1c***) was cycled down to 0.5 V vs Li^+/Li and studied by galvanostatic cycling at charge/discharge rates from 1 C to 20 C. **Figure 7a** shows that this version of the nanocomposite holds a specific capacity of 1302 mAh/g at a charging rate of 1 C (21.2 $\mu A/cm^2$), while 80.2 % of the total capacity is pseudocapacitance attributed mainly to the amorphous matrix (see **S9** for calculation). Though this is a complex system and it is challenging to assign a capacity to the amorphous component of this multi-phase system, we have *estimated* the specific capacity of the amorphous phase itself to be between 1500-1679 mAh/g by calculating the relative wt. % of each phase (anatase TiO_2, orthorhombic LTP, and amorphous LTP) through Rietvelt refinement and dQ/dV integration. For more information on how we arrived at this estimate, see **S10**. This behavior (high energy density

observed as pseudocapacitance) is common in amorphous metal phosphate anodes (i.e., $V_2O_5 \bullet P_2O_5$, $SnO_2 \bullet P_2O_5$) that have demonstrated a high capacity for Li^+ ion storage at low potentials (ranging from 500 - 1650 mAh/g depending on chemistry and microstructure).[39,40] Of note, previous work on the $V_2O_5 \bullet P_2O_5$ system has demonstrated that nanostructuring the glass anodes with embedded electronic conductors like reduced graphene oxide (rGO) plays an important role in increasing the coulombic efficiency of the first cycle. This strategy shows a ~66 % increase in stable capacity in $75V_2O_5 \bullet 25P_2O_5$ coated with rGO on particle diameters on the order of microns.[39] Our LTP system takes this approach to the nanoscale in which both the film thickness (60 nm) and the electronic conductor (TiO2, 5-40 nm diameter)[15] operate at very small feature sizes. This provides plenty of pathways for Li^+ insertion and extraction and reduces diffusion limitations in the system as suggested by Kebede et. al., that could result in much higher capacity retention.

With increased current density, up to a charging rate of 20 C (414 $\mu A/cm^2$), the specific capacity of the system steadily decreases down to 807 mAh/g (61.9 % of initial state). The 8 % drop in rate retention at 20 C in this extended voltage window compared to the case in **Figure 6** with orthorhombic LTP grains is more than compensated for by the 312 % increase in capacity provided by the amorphous matrix accepting large amounts of Li^+ at low potentials. As the gradual slope of the charge-discharge curves in **Figure 7b** suggests, most of the lithium enters the system as a solid-solution particularly at lower potentials. When cycled down to 0.5 V vs Li^+/Li, this ALD nanocomposite has good phase reversibility with high specific capacity, making it a promising microbattery anode material.

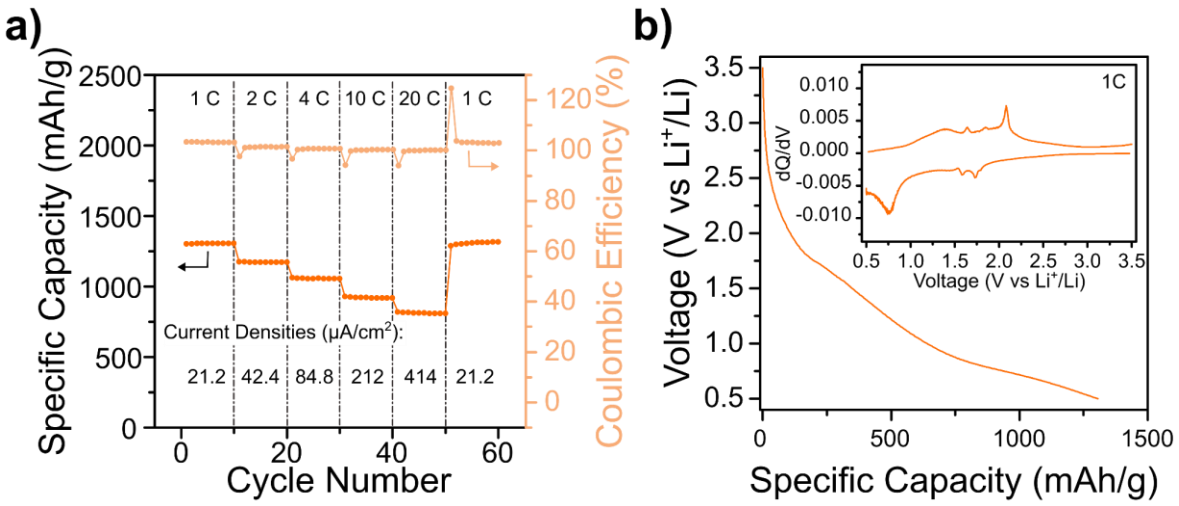

Figure 7. a) Rate retention results for Li-Ti-P-O (Li-poor) annealed at 650 °C for 8.5 minutes cycled in a T-cell vs lithium metal in 1M $LiClO_4$ in PC liquid electrolyte between 0.5 V – 3.5 V at charging rates of 1C (21.2 μA/cm²), 2C (42.4 μA/cm²), 4C (84.8 μA/cm²), 10C (212 μA/cm²), and 20 C (414 μA/cm²). b) Galvanostatic discharge curve of the 10th cycle in the series for 1 C. The inset is a representative dQ/dV curve of this voltage window taken from the 1 C discharge curve.

3.4.4 Isolation of Crystalline Orthorhombic LTP Grain Effects on Fast Charging Behavior

As indicated by the lack of redox activity above 2.1 V vs Li^+/Li in the charge-discharge curves and dQ/dV of **Figure 7b**, this nanocomposite no longer contains the orthorhombic LTP crystalline phase, which has been replaced by a sluggish $Li_{3+x}Ti_2(PO_4)_3$ phase. We can use this as a control to directly study the effects of the orthorhombic phase on the kinetics of this materials system. This was done by cycling films with orthorhombic LTP grains (as in ***Scheme 1b***) and without orthorhombic LTP grains (as in ***Scheme 1c***) in the voltage window where only the orthorhombic LTP structure should be redox active (2.1 V – 3.5 V vs Li^+/Li). As expected, the dQ/dV (**S13**) of the sample with orthorhombic LTP grains shows redox peaks at 2.8, 2.45, and 2.25 V vs Li^+/Li like in **Figure 2** that indicate Li^+ ion insertion/extraction into/from the orthorhombic LTP phase.[20] Likewise, the sample without orthorhombic LTP grains (that were electrochemically removed) displays no redox behavior within this voltage window (**S13**). It instead demonstrates

only pseudocapacitance behavior which is due to a combination of surface capacitance contributions as well as solid-solution Li^+ ion insertion into the amorphous LTP matrix.[41]

Figure 8a shows the rate retention experiment performed on both nanocomposite films (with and without orthorhombic LTP grains) in which the current density of both samples increased every 10 cycles up to 332 $\mu A/cm^2$ for a nominal charging rate of 200 C (18 seconds). The film without orthorhombic LTP has an initial capacity of 166 mAh/g, but it sees a 79 % drop in specific capacity at 200 C (down to 27 mAh/g). In contrast, the sample with orthorhombic LTP grains has an initial capacity of 125 mAh/g at a charging rate of 1 C and retains 60 % of its capacity at a nominal charging rate of 200 C (75 mAh/g).

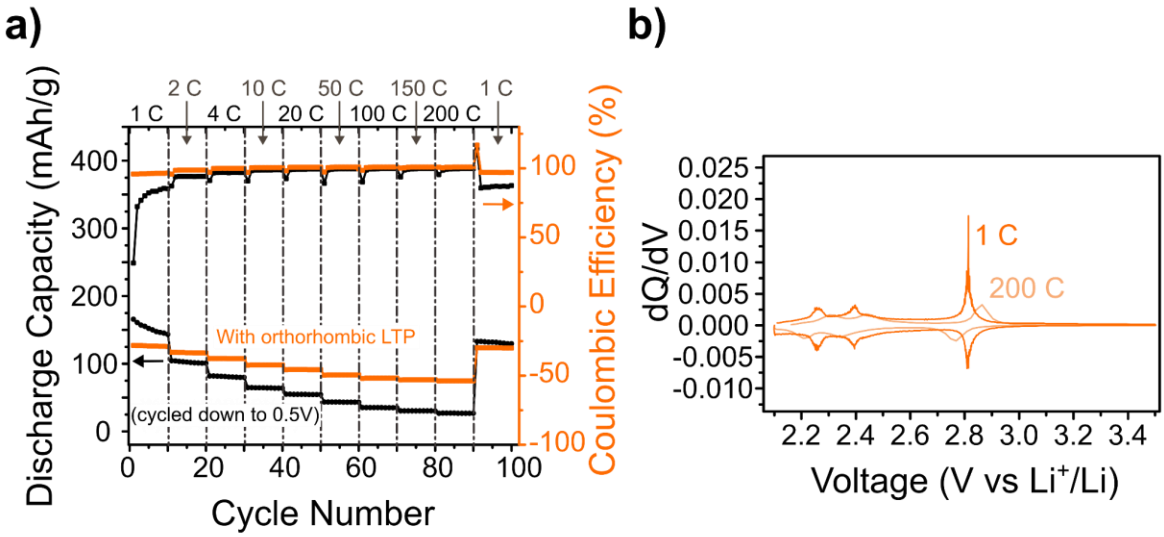

Figure 8. a) Rate retention results for Li-Ti-P-O (Li-poor) films annealed at 650 °C for 8.5 minutes with orthorhombic LTP grains (orange) and without orthorhombic LTP grains (black) cycled in a beaker cell vs lithium metal in 1 M $LiClO_4$ in PC liquid electrolyte between 2.1 V – 3.5 V at charging rates of 1C (1.66 $\mu A/cm^2$), 2C (3.32 $\mu A/cm^2$), 4C (6.64 $\mu A/cm^2$), 10C (16.6 $\mu A/cm^2$), 20 C (33.2 $\mu A/cm^2$), 50 C (83 $\mu A/cm^2$), 100 C (166 $\mu A/cm^2$), 150 C (249 $\mu A/cm^2$), and 200 C (332 $\mu A/cm^2$). b) dQ/dV of the nanocomposite with orthorhombic LTP grains cycled at 1 C and 200 C.

Thus far, the orthorhombic LTP redox peaks have demonstrated minimal polarization upon cycling at slower rates compared to the other redox active phases like anatase TiO_2 and the

$Li_{3+x}Ti_2(PO_4)_3$ phase. The orthorhombic LTP redox peaks demonstrate more notable polarization (100 mV peak to peak separation) at faster charging rates (200 C) as shown in **Figure 8b**. The nearly identical polarization of each peak (2.25, 2.45, and 2.8 V vs Li^+/Li) at fast charging rates indicates that each electron transfer event has similar kinetics. The orthorhombic LTP phase in the nanocomposite provides a fast-kinetics pathway for Li^+ ion insertion and conduction that is lost when the orthorhombic LTP grains are electrochemically removed by applying low potentials (<0.5 V vs Li^+/Li). In general, improved rate performance of nanocomposite electrode materials can come from high surface area and short diffusion distances provided by nanoscale particle sizes, sufficient electron conduction at the reaction sites, and decreased diffusion lengths over the entire film.[42] By making this direct comparison where the film thicknesses are identical but the nanoparticle content and distribution differs (with and without orthorhombic LTP, electrochemically removed), we can attribute the fast kinetics of the nanocomposite to the ultra-fast kinetics of the orthorhombic LTP structure itself.

4. Conclusions and Outlook

In this work, we demonstrated electrochemical phase engineering as an experimental lever for systematically controlling phase distribution and isolating the transport contributions of individual phases in a complex quaternary nanocomposite. By combining composition-controlled ALD films with voltage-window-selective cycling, we drove controlled evolution of crystal structure, phase distribution, and internal interfaces in the Li–Ti–P–O system — extending the concept of electrochemical phase engineering from prior demonstrations in other thin film systems[22] to a materials platform with direct compositional tunability and structural phase selectivity at multiple stages of processing.

The specific influence of the crystalline LTP phase on kinetic behavior was isolated directly by comparing films with and without LTP grains in the voltage window where only the crystalline LTP phase is redox active (i.e., 2.1 V – 3.5 V vs Li^+/Li). Films without crystalline LTP retained only 21 % of their capacity at an ultrafast charging rate of 200 C, whereas films with crystalline LTP retained 60 % at the same rate. We attribute this difference in fast-rate capacity retention directly to the fast kinetics of the crystalline LTP phase, isolated here using electrochemical phase engineering as a controlled experimental lever, and supported by the intimate interfacial contact provided by the amorphous phosphate matrix between crystalline grains.

This work showcases how to control materials properties of a quaternary materials system like Li-Ti-P-O by selecting the right combination of annealing and redox potentials to promote high power density and high energy density ripe for advancements in new classes of thin film ionic devices. Beyond these specific performance attributes, this work demonstrates that the Li–Ti–P–O nanocomposite is a versatile platform in which phase composition, grain boundary character, and interface structure can be varied — through ALD process parameters, thermal annealing conditions, or electrochemical modification — to study how each phase governs mixed ionic-electronic transport at the nanoscale.

Supporting Information

- SEM and XRR used to calculate the film thickness and film density for gravimetric studies.
- XPS survey and high resolution spectra used to calculate the compositional breakdown of the films in this study.
- More detailed diagrams and description of the T-cell electrochemical setup.

- EIS and DC Relaxation of an as-deposited amorphous film showing evidence of the starting morphology of the film.
- Description of dQ/dV integration calculations mentioned throughout this work to understand the contributions to the capacity of the different phases in the nanocomposites.
- Description of dQ/dV integration used to estimate the contribution to the capacity of the amorphous matrix.
- dQ/dV of samples with and without orthorhombic LTP cycled between 2.1 V - 3.5 V vs Li^+/Li.
- Long-term cycling behavior of Li-poor film cycled from 1.2 V - 3.5 V vs Li^+/Li.

Data Availability

All data will be accessible on the Digital Repository at the University of Maryland (DRUM).

Corresponding Authors:

Keith E. Gregorczyk: kgregorc@umd.edu

Daniela R. Fontecha: drfontec@umd.edu

Author Contributions

K.E.G., G.W.R., and D.R.F. developed the plans for research. D.R.F. developed the ALD process, fabricated devices, and characterized the films. K.E.G., G.W.R., N.K., and S.B.L. provided guidance in the planning of experiments and interpretation of results. O.G. developed the in-house synthesis of the lithium ALD precursor (lithium *tert*-butoxide) required to deposit LTP films. D.R.F. wrote the manuscript with input from all authors. All authors approved the final manuscript.

Funding Sources

This work was supported by the U.S. Department of Energy Office of Science, Basic Energy Sciences, under Grant DE-SC0021070, encompassing and emphasizing the synthesis of Li containing titanium phosphates with composition and structure varied through a dopant supercycle process and corresponding electrochemical analysis. D.R.F. was supported by the National Science Foundation Graduate Research Fellowship Program under Grant No. DGE 1840340. Any opinions, findings, and conclusions or recommendations expressed in this material are those of the author(s) and do not necessarily reflect the views of the National Science Foundation.

Acknowledgements:

The authors would like to acknowledge the Zitoun research group at Bar-Ilan University for their contributions to this work in the form of XRR measurements used to estimate the film densities and calculate the mass of the samples.

References

(1) Pearse, A.; Schmitt, T.; Sahadeo, E.; Stewart, D. M.; Kozen, A.; Gerasopoulos, K.; Talin, A. A.; Lee, S. B.; Rubloff, G. W.; Gregorczyk, K. E. Three-Dimensional Solid-State Lithium-Ion Batteries Fabricated by Conformal Vapor-Phase Chemistry. *ACS Nano* **2018**, *12* (5), 4286–4294. https://doi.org/10.1021/acsnano.7b08751.

(2) Ahuja, K.; Sallaz, V.; Nuwayhid, R. B.; Voiron, F.; McCluskey, P.; Rubloff, G. W.; Gregorczyk, K. E. Ultra-Thin on-Chip ALD LiPON Capacitors for High Frequency Application. *J. Power Sources* **2023**, *575*, 233056. https://doi.org/10.1016/j.jpowsour.2023.233056.

(3) Warecki, Z.; Ferrari, V. C.; Robinson, D. A.; Sugar, J. D.; Lee, J.; Ievlev, A. V.; Kim, N. S.; Stewart, D. M.; Lee, S. B.; Albertus, P.; Rubloff, G.; Talin, A. A. Simultaneous Solid Electrolyte Deposition and Cathode Lithiation for Thin Film Batteries and Lithium Iontronic Devices. *ACS Energy Lett.* **2024**, *9* (5), 2065–2074. https://doi.org/10.1021/acsenergylett.4c00674.

(4) Li, T.; Xiao, K. Solid-State Iontronic Devices: Mechanisms and Applications. *Adv. Mater. Technol.* **2022**, *7* (12), 1–17. https://doi.org/10.1002/admt.202200205.

(5) Pérez-Mitta, G.; Albesa, A. G.; Trautmann, C.; Toimil-Molares, M. E.; Azzaroni, O. Bioinspired Integrated Nanosystems Based on Solid-State Nanopores: “Iontronic” Transduction of Biological, Chemical and Physical Stimuli. *Chem. Sci.* **2017**, *8* (2), 890–913. https://doi.org/10.1039/c6sc04255d.

(6) Maier, J. Nanoionics: Ion Transport and Electrochemical Storage in Confined Systems. *Nat. Mater.* **2005**, *4* (11), 805–815. https://doi.org/10.1038/nmat1513.

(7) Jung, Y. S.; Cavanagh, A. S.; Riley, L. A.; Kang, S.; Dillon, A. C.; Groner, M. D.; George, S. M.; Lee, S. Ultrathin Direct Atomic Layer Deposition on Composite Electrodes for Highly Durable and Safe Li-Ion Batteries. *Adv. Mater.* **2010**, *22* (19), 2172–2176. https://doi.org/10.1002/adma.200903951.

(8) Wang, H.; Hoang, B.; Wang, F.; Liou, S.-C.; Wang, C.; Rubloff, G.; Lin, C.-F. Oversaturated Li-FeOF Solid Solutions Developed Using LiPON Interfacial Coating. *Mater. Adv.* **2025**, *6* (17), 5892–5900. https://doi.org/10.1039/D5MA00338E.

(9) Elam, J. W.; Baker, D. A.; Hryn, A. J.; Martinson, A. B. F.; Pellin, M. J.; Hupp, J. T. Atomic Layer Deposition of Tin Oxide Films Using Tetrakis(Dimethylamino) Tin. *J. Vac. Sci. Technol. Vac. Surf. Films* **2008**, *26* (2), 244–252. https://doi.org/10.1116/1.2835087.

(10) Chen, X.; Pomerantseva, E.; Banerjee, P.; Gregorczyk, K.; Ghodssi, R.; Rubloff, G. Ozone-Based Atomic Layer Deposition of Crystalline V_2 O_5 Films for High Performance Electrochemical Energy Storage. *Chem. Mater.* **2012**, *24* (7), 1255–1261. https://doi.org/10.1021/cm202901z.

(11) Song, G. Y.; Oh, C.; Sinha, S.; Son, J.; Heo, J. Facile Phase Control of Multivalent Vanadium Oxide Thin Films (V_2 O_5 and VO_2) by Atomic Layer Deposition and Postdeposition Annealing. *ACS Appl. Mater. Interfaces* **2017**, *9* (28), 23909–23917. https://doi.org/10.1021/acsami.7b03398.

(12) Xie, M.; Sun, X.; Zhou, C.; Cavanagh, A. S.; Sun, H.; Hu, T.; Wang, G.; Lian, J.; George, S. M. Amorphous Ultrathin TiO_2 Atomic Layer Deposition Films on Carbon Nanotubes as Anodes for Lithium Ion Batteries. *J. Electrochem. Soc.* **2015**, *162* (6), A974–A981. https://doi.org/10.1149/2.0501506jes.

(13) Wang, B.; Liu, J.; Sun, Q.; Xiao, B.; Li, R.; Sham, T.; Sun, X. Titanium Dioxide/Lithium Phosphate Nanocomposite Derived from Atomic Layer Deposition as a High-Performance Anode for Lithium Ion Batteries. *Adv. Mater. Interfaces* **2016**, *3* (21), 1600369. https://doi.org/10.1002/admi.201600369.

(14) Liu, J.; Banis, M. N.; Sun, Q.; Lushington, A.; Li, R.; Sham, T.; Sun, X. Rational Design of Atomic-Layer-Deposited $LiFePO_4$ as a High-Performance Cathode for Lithium-Ion Batteries. *Adv. Mater.* **2014**, *26* (37), 6472–6477. https://doi.org/10.1002/adma.201401805.

(15) Fontecha, D. R.; Kozen, A. C.; Stewart, D. M.; Hall, A. T.; Cumings, J.; Rubloff, G. W.; Gregorczyk, K. E. Nanoscale Mixed Ion-Electron-Conducting NASICON-Type Thin Films: Lithium Titanium Phosphate via Atomic Layer Deposition. *ACS Appl. Mater. Interfaces* **2025**, *17* (17), 25358–25369. https://doi.org/10.1021/acsami.5c02201.

(16) Gomez, O. J.; Antar, A.; Hall, A. T.; Tapia-Aracayo, L.; Seo, J.; Kim, N.; Sun, Z.; Lim, R.; Chen, F.; Li, Y.; Cumings, J.; Rubloff, G.; Lee, S. B.; Stewart, D.; Wang, Y. A Facile Synthesis of Bulk LiPON in Solution for Solid-State Electrolytes. *J. Mater. Chem. A* **2025**, *13* (34), 28368–28376. https://doi.org/10.1039/D5TA03196F.

(17) Balachandran, U.; Eror, N. G. Raman Spectra of Titanium Dioxide. *J. Solid State Chem.* **1982**, *42* (3), 276–282. https://doi.org/10.1016/0022-4596(82)90006-8.

(18) Giarola, M.; Sanson, A.; Tietz, F.; Pristat, S.; Dashjav, E.; Rettenwander, D.; Redhammer, G. J.; Mariotto, G. Structure and Vibrational Dynamics of NASICON-Type $LiTi_2$ $(PO_4)_3$. *J. Phys. Chem. C* **2017**, *121* (7), 3697–3706. https://doi.org/10.1021/acs.jpcc.6b11067.

(19) Wang, B.; Greenblatt, M.; Wang, S.; Hwu, S. J. Ionic Conductivity of Lithium Titanium Phosphate Li1+xTi2 (PO4)3(0.2 < x < 1.72) with NASICON-Related Structures. *Chem. Mater.* **1993**, *5* (1), 23–26. https://doi.org/10.1021/cm00025a008.

(20) Kee, Y.; Dimov, N.; Minami, K.; Okada, S. Orthorhombic Lithium Titanium Phosphate as an Anode Material for Li-Ion Rechargeable Battery. *Electrochimica Acta* **2015**, *174*, 516–520. https://doi.org/10.1016/j.electacta.2015.06.032.

(21) Delmas, C.; Nadiri, A.; Soubeyroox, J. L. The NASICON-Type Titanium Phosphates ATi2(PO4)3 (A = Li, Na) as Electrode Materials. *Solid State Ion.* **1988**, *28–30*, 419–423.

(22) Sun, Z.; Kim, N. S.; Tiwari, R.; Zitoun, D.; Rubloff, G. W.; Lee, S. B.; Gregorczyk, K. E. Electrochemical Phase Engineering of Γ′-V_2O_5 Thin Films for Sodium-Ion Storage Electrodes. *ACS Omega* **2025**, *10* (50), 61414–61421. https://doi.org/10.1021/acsomega.5c06197.

(23) Srout, M.; Lasri, K.; Dahbi, M.; Kara, A.; Tetard, L.; Saadoune, I. Understanding of the Li-Insertion Process in a Phosphate Based Electrode Material for Lithium Ion Batteries. *J. Power Sources* **2019**, *435*, 226803. https://doi.org/10.1016/j.jpowsour.2019.226803.

(24) Laskova, B.; Frank, O.; Zukalova, M.; Bousa, M.; Dracinsky, M.; Kavan, L. Lithium Insertion into Titanium Dioxide (Anatase): A Raman Study with$^{16/18}$ O and$^{6/7}$ Li Isotope Labeling. *Chem. Mater.* **2013**, *25* (18), 3710–3717. https://doi.org/10.1021/cm402056j.

(25) Shan, W.; Chen, J.; Wei, X.; Chowdari, B. V. R.; Wu, X.; Wen, Z. Enhancing the Dendritic-Tolerance of NASICON-Based Electrolytes by Grain Boundary Engineering. *ACS Appl. Mater. Interfaces* **2025**, *17* (40), 56144–56152.

(26) Zachauchristiansen, B.; West, K.; Jacobsen, T.; Atlung, S. Lithium Insertion in Different TiO2 Modifications. *Solid State Ion.* **1988**, *28–30*, 1176–1182. https://doi.org/10.1016/0167-2738(88)90352-9.

(27) Subramanian, V.; Karki, A.; Gnanasekar, K. I.; Eddy, F. P.; Rambabu, B. Nanocrystalline TiO2 (Anatase) for Li-Ion Batteries. *J. Power Sources* **2006**, *159* (1), 186–192. https://doi.org/10.1016/j.jpowsour.2006.04.027.

(28) Yao, X.; Su, Z.; Pan, H. Synthesis and Electrochemical Properties of Nonstoichiometric Composition Li2.7Ti2(PO4)3/C with Orthorhombic Structure. *Chem. Phys. Lett.* **2016**, *659*, 88–92. https://doi.org/10.1016/j.cplett.2016.07.014.

(29) Wang, S.; Hwu, S. J. A New Series of Mixed-Valence Lithium Titanium(III/IV) Phosphates, Li1+xTi2(PO4)3 (0 < x < 2), with NASICON-Related Structures. *Chem. Mater.* **1992**, *4* (3), 589–595. https://doi.org/10.1021/cm00021a018.

(30) Aatiq, A.; Ménétrier, M.; Croguennec, L.; Suard, E.; Delmas, C. On the Structure of $Li_3Ti_2(PO_4)_3$. *J Mater Chem* **2002**, *12* (10), 2971–2978. https://doi.org/10.1039/B203652P.

(31) Boireau, A.; Soubeyroux, J. L.; Olazcuaga, R.; Delmas, C.; Le Flem, G. Li Intercalation in CuII0.5Ti2(PO4)3: A Neutron Diffraction Study of Li3.5Cu0.5Ti2(PO4)3. *Solid State Ion.* **1993**, *63–65*, 484–487. https://doi.org/10.1016/0167-2738(93)90148-V.

(32) Aatiq, A.; Delmas, C.; El Jazouli, A. Structural and Electrochemical Study of Li0.5Mn0.5Ti1.5Cr0.5(PO4)3. *J. Solid State Chem.* **2001**, *158* (2), 169–174. https://doi.org/10.1006/jssc.2001.9088.

(33) El-Shinawi, H.; Janek, J. Low-Temperature Synthesis of Macroporous $LiTi_2(PO_4)_3$/C with Superior Lithium Storage Properties. *RSC Adv.* **2015**, *5* (19), 14887–14891. https://doi.org/10.1039/C4RA16155F.

(34) Aatiq, A.; Delmas, C.; Jazouli, A. E.; Gravereau, P. Structure and Electrochemical Study of Li2xMn(1-x)TiCr(PO4)3 (X=0-0.5) with NASICON-like Structure. *Ann. Chim. Sci. Matér.* **1998**, *23* (1–2), 121–124.

(35) Huang, Z.; Liu, L.; Zhou, Q.; Tan, J.; Yan, Z.; Xia, D.; Shu, H.; Yang, X.; Wang, X. Carbon-Coated Lithium Titanium Phosphate Nanoporous Microplates with Superior Electrochemical Performance. *J. Power Sources* **2015**, *294*, 650–657. https://doi.org/10.1016/j.jpowsour.2015.06.143.

(36) Santos, D. A.; Rezaei, S.; Zhang, D.; Luo, Y.; Lin, B.; Balakrishna, A. R.; Xu, B.-X.; Banerjee, S. Chemistry–Mechanics–Geometry Coupling in Positive Electrode Materials: A Scale-Bridging Perspective for Mitigating Degradation in Lithium-Ion Batteries through Materials Design. *Chem. Sci.* **2023**, *14* (3), 458–484. https://doi.org/10.1039/D2SC04157J.

(37) Wang, G. X.; Bradhurst, D. H.; Dou, S. X.; Liu, H. K. LiTi2(PO4)3 with NASICON-Type Structure as Lithium-Storage Materials. *J. Power Sources* **2003**, *124* (1), 231–236. https://doi.org/10.1016/S0378-7753(03)00609-8.

(38) Haregewoin, A. M.; Leggesse, E. G.; Jiang, J.-C.; Wang, F.-M.; Hwang, B.-J.; Lin, S. D. Comparative Study on the Solid Electrolyte Interface Formation by the Reduction of Alkyl Carbonates in Lithium Ion Battery. *Electrochimica Acta* **2014**, *136*, 274–285. https://doi.org/10.1016/j.electacta.2014.05.103.

(39) Kebede, M. A.; Palaniyandy, N.; Ramadan, R. M.; Sheha, E. The Electrical and Electrochemical Properties of Graphene Nanoplatelets Modified 75V2O5–25P2O5 Glass as a Promising Anode Material for Lithium Ion Battery. *J. Alloys Compd.* **2018**, *735*, 445–453. https://doi.org/10.1016/j.jallcom.2017.11.136.

(40) Shang, C.; Li, X.; Wei, R.; Liu, X.; Xu, S.; Zhang, J. Research Progress of Metal Oxide Glass Anode Materials for Lithium-Ion Batteries: A Review. *J. Non-Cryst. Solids* **2023**, *618*, 122547. https://doi.org/10.1016/j.jnoncrysol.2023.122547.

(41) Huggins, R. A. *Advanced Batteries*; Springer US: Boston, MA, 2009. https://doi.org/10.1007/978-0-387-76424-5.

(42) Luo, J. -Y.; Xia, Y. -Y. Aqueous Lithium-ion Battery $LiTi_2(PO_4)_3$ /$LiMn_2O_4$ with High Power and Energy Densities as Well as Superior Cycling Stability**. *Adv. Funct. Mater.* **2007**, *17* (18), 3877–3884. https://doi.org/10.1002/adfm.200700638.